Proceedings of the ASME 2013 32nd International Conference on Ocean, Offshore and Arctic Engineering
OMAE2013
June 9-14, 2013, Nantes, France

OMAE2013-11277

DAMAGE AND FAILURE IN AN X65 STEEL PIPELINE CAUSED BY TRAWL GEAR IMPACT

Martin Kristoffersen*
Tore Børvik
Magnus Langseth
Odd Sture Hopperstad
Structural Impact Laboratory (SIMLab)
Centre for Research-based Innovation (CRI)
Department of Structural Engineering
Norwegian University of Science and Technology
Rich. Birkelands vei 1, NO-7491 Trondheim, Norway
E-mail: martin.kristoffersen@ntnu.no

Håvar Ilstad
Erik Levold
Statoil ASA
Research Centre Trondheim
Marine Facilities and Pipeline Technology
Pb. 2470, NO-7053 Ranheim, Norway
E-mail: hil@statoil.com

ABSTRACT

Offshore pipelines subjected to accidental impact loads from trawl gear or anchors may experience large global deformations and large local strains, creating a complex stress and strain history. In this study experiments and numerical simulations have been carried out to investigate the impact of a pipeline which is subsequently hooked and released. Material and component tests have been performed to investigate the behaviour during impact, and to observe if/when fracture occurs. The pipes were first impacted in a pendulum accelerator at varying velocities before they were pulled straight in a tension machine. Fracture was found in the impacted area of all the pipes during straightening. Material tests were done to determine the characteristics of the X65 grade steel. Numerical simulations showed excellent compliance with the impact phase, while the load level in the stretching phase was a bit overestimated.

INTRODUCTION

Transportation of oil and gas is an essential part of the offshore industry. To this end, pipelines are under widespread use, often under high pressures and temperatures [1,2]. Impacts from trawl gear and anchors are known to cause problems, see e.g. [3]. Occurances like these necessitate assessments regarding the hazards and potential damage arising from such events [4], as failure in a pipeline transporting oil and/or gas could result in severe environmental and economic damage.

Det Norske Veritas (DNV) has published a standard on general design of pipeline systems [5] and specified some recommended practice on interference between pipelines and trawl gear [6]. The latter of these provides a critical load of a trawl clump weight of 9000 kg impacting the pipeline at 2.8 m/s. It also includes pull-over as well as possible hooking analysis. A load cycle of impact, hooking, pull-over and release produces a complex stress and strain history which is not particularly well covered in the guidelines. In addition to the simplified analysis, the guidelines allow for use of numerical analyses and model tests in the design phase.

The open literature provides several studies on pipeline impact. Johnson, Reid and coworkers published a series of papers on large transverse deformations of thin walled circular tubes [7, 8, 9]. The first of these [7] also contain impact tests where a wedge was dropped onto the pipe's midspan. Fully clamped pipes have been studied by Jones et al. [10], and inclusion of pressure in pipelines has also been investigated [11].

*Corresponding author

Manes et al. [2] attempted to recreate the loading sequence of impact, pull-over and subsequent release by subjecting plate strips of an actual offshore pipeline to quasi-static three point bending tests. The strips were then pulled straight and checked for fracture.

This study presents impact experiments on a simply supported pipe made from X65 steel, a material typically used for offshore pipelines transporting oil and gas [12]. A pendulum accelerator (described in detail in [13]) was used to launch a trolley with a given mass and velocity against the pipe. No surrounding water was present, and no internal pressure was applied to the pipe. After the impact event the pipeline was pulled straight in a tension rig. This is thought to be a simplification of the loading sequence of impact and straightening of a full-scale pipeline. Finally, simulations of both the impact and subsequent stretching of the pipe were carried out using a finite element model. The impact phase was captured very well, whereas the observed fracture in the component tests were not captured in the analyses.

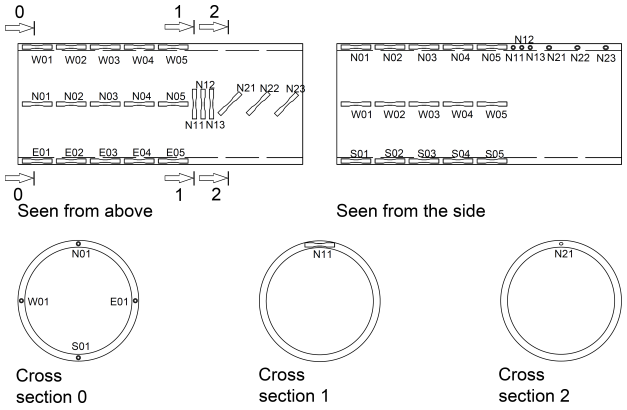

FIGURE 1. LOCATIONS AND DIRECTIONS FROM WHICH TEST SPECIMENS WERE CUT. NOTE THAT NOT ALL SPECIMENS INDICATED ON THE FIGURE WERE USED IN THE MATERIAL TEST PROGRAMME PRESENTED IN THIS STUDY.

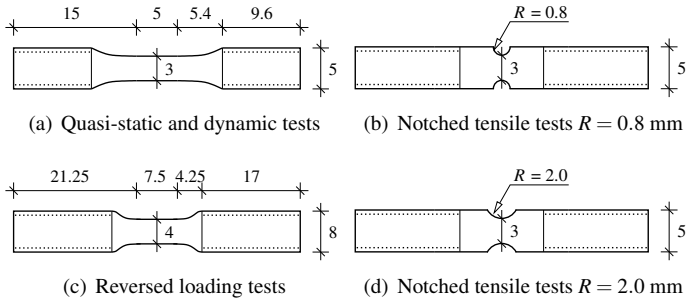

FIGURE 2. SPECIMEN GEOMETRIES USED IN THE MATERIAL TEST PROGRAMME.

MATERIAL TESTS

Material description

The material in the pipes used in this study is similar to the X65 grade steel used by Manes et al. [2], but the pipes are manufactured in a different manner. Where the pipes used in [2] were formed from rolled plates and welded longitudinally, the current pipes are made seamless [14]. The production of the pipeline was in accordance with the guidelines in DNV-OS-F101 [5] by the Argentinean supplier Tenaris. A different production method may give rise to different material properties, hence a material test programme was conducted as described below.

All specimens used in the material tests (and in the component tests presented later) were taken from the same continuous pipe, which had an initial length of 12 m. According to the material inspection certificate, the nominal yield stress and the ultimate tensile strength are 450 MPa and 535 MPa, respectively. Young's modulus is 208000 MPa. The inner diameter of the pipe is 123 mm, and the nominal wall thickness 9.5 mm, making the outer diameter 142 mm and the diameter to thickness ratio approximately 13. Aside from Fe, the main chemical constituents of this alloy are 0.09 C, 0.25 Si, 1.13 Mn, 0.04 Cr, 0.09 Mo, 0.09 Cu and 0.06 V (numbers in weight percentage).

Experimental programme

The pipe material's cross-section homogeneity, possible anisotropic yielding properties, isotropic versus kinematic hardening behaviour, strain rate sensitivity and failure properties were the sought characteristics. To examine the section homogeneity, tensile specimens were cut from different locations – dubbed north, south, east and west – across the cross-section of the pipe. Being seamless, the pipe has no natural reference point on the cross-section, so one was chosen at random. As the material may have anisotropic properties, specimens were cut in three different directions with respect to the pipe's longitudinal axis; 0°, 45° and 90°. Figure 1 makes evident the positions and directions from where the specimens were cut. These specimens were tested quasi-statically in tension, along with specimens of two different notch root radii ($R = 0.8$ mm and $R = 2.0$ mm). Two specimens from each position and direction were tested, and three specimens of each notch root radii.

As will be discussed later, the cross-section did indeed appear to be homogenous, and no anisotropic material behaviour seemed to be present. With this in mind, the location for further material tests became of no significant importance. Tests at elevated strain rates were done on the same specimen geometry as for the quasi-static tension tests, while a slightly different geometry was used for the specimens in the tests involving reversed loading. An overview of the material test programme is given in Table 1, while the specimen geometries are shown in Fig. 2.

TABLE 1. OVERVIEW OF MATERIAL TEST PROGRAMME.

Quasi-static tensile tests

Geometry	*Specimens*							
Fig. 2(a)	N01	N02	E01	E02	S01	S02	W01	W02
	N11	N12	N21	N22				
Fig. 2(b)		R08-1		R08-2		R08-3		
Fig. 2(d)		R20-1		R20-2		R20-3		

Dynamic tensile tests

Geometry	*Specimens and accompanying true strain rates in [s^{-1}]*					
Fig. 2(a)	E04	E05	W04	W05	N04	S04
	234	242	545	527	820	838

Reversed loading tests

Geometry	*Loading direction and levels of deformation (% strain)*									
Fig. 2(c)	**TC**	0.0	0.4	1.0	1.5	2.0	4.0	5.0	6.0	8.0	10.0
	CT	-	-	1.0	1.5	2.0	4.0	5.0	-	-	-

Uniaxial tensile tests

Tensile tests were carried out at quasi-static strain rate and room temperature on smooth axisymmetric specimens, whose geometry can be seen in Fig. 2(a). A displacement controlled Zwick testing machine was used with a constant deformation rate of 0.3 mm/min, corresponding to an initial strain rate of $\dot{\varepsilon} = 10^{-3}$ s^{-1}. Two tests from each of the positions across the cross-sections (north, south, etc.) and from each of the directions (0°, 45° and 90°) were performed.

During testing, the force, the cross-head displacement and the specimen's diameter reduction were measured. A laser-based measuring device was used to measure the diameter reduction at the minimum cross-section until fracture. Two perpendicular lasers (AEROEL XLS13XY with 1 μm resolution) continuously executed the measuring with great accuracy. The lasers were mounted on a mobile frame to ensure that the diameters were always measured at minimum cross-section. With diameter reduction measurements it is possible to calculate the true stress σ and the true logarithmic strain ε through the formulas

$$\sigma = \frac{F}{A} \tag{1}$$

$$\varepsilon = \ln\left(\frac{A_0}{A}\right) \tag{2}$$

in which F is the force measured by the load cell on the Zwick machine and A_0 is the specimen's initial cross-sectional area calculated by $A_0 = (\pi/4)D_0^2$, D_0 being the initial diameter. A is the current area of the cross-section, obtained by $A = (\pi/4)D_1D_2$ where D_1 and D_2 are the diameters measured by the two lasers. Assuming additive decomposition of the elastic and plastic strains, the plastic strain can be found through the relation $\varepsilon^p = \varepsilon - \sigma/E$ where E is Young's modulus. It should be noted that plastic incompressibility and negligible elastic strains are assumed in Eqn. (2), and that the measured true stress σ is equal to the major principal stress σ_1 in the uniaxial tension test.

Results from the section homogeneity tests (N, S, E, W) are presented in Fig. 3(a), plotted as true stress vs. true strain. The scatter between each individual test from each position was low, and the same applies to the tests in different directions with respect to the pipe's longitudinal axis. True stress-true strain relations from the directional tests (0°, 45°, 90°) are displayed in Fig. 3(b).

Based on average values from 12 tests, the material yields at 478 ± 15 MPa and has a nominal peak stress of 572 ± 14 MPa. It strain hardens to a true peak stress of 1314 ± 12 MPa and fails at a true strain of 1.61 ± 0.03 by a ductile cup-and-cone fracture. The data from the tests strongly suggest that for practical and design applications the material properties are isotropic and homogenous, in contrast to the quite anisotropic appearance of the X65 steel used in [2].

Tests on notched specimens with two different notch root radii (see Figs. 2(b) and (d)) were also performed. Data from the tests are presented in Fig. 3(c), which shows one typical curve for each notch radius. The stress triaxiality σ^* is defined as the ratio between the hydrostatic stress σ_H and the von Mises equivalent stress σ_{eq},

$$\sigma^* = \frac{\sigma_H}{\sigma_{eq}} \tag{3}$$

As different areas of the pipe undergo different types of deformations, the stress triaxiality is bound to vary, thus necessitating data at varying triaxialities. The fracture strain clearly decreased when the notch became sharper and the stress triaxiality increased. The stress at fracture, however, appears to be much less affected by the notch which is an interesting characteristic. More details can be found in [15].

Dynamic tensile tests

A split-Hopkinson tension bar (SHTB) [16] was used to obtain stress-strain relations at elevated strain rates. Two tests at three different true strain rates were carried out; 240 s^{-1}, 535 s^{-1} and 830 s^{-1}. Figure 4(a) shows that the flow stress increased with increasing strain rate, while the fracture strain remained of the same order, about 1.6. The component tests are dynamic in

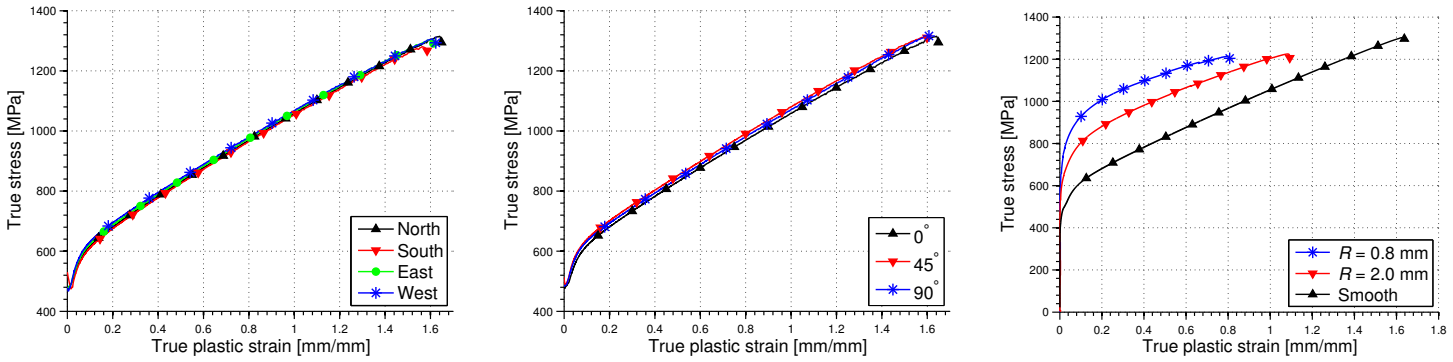

(a) Section homogeneity (b) Anisotropy (c) Notched tests

FIGURE 3. TRUE STRESS-TRUE STRAIN DATA FROM QUASI-STATIC TENSILE TESTS ON UNIAXIAL AND NOTCHED SPECIMENS.

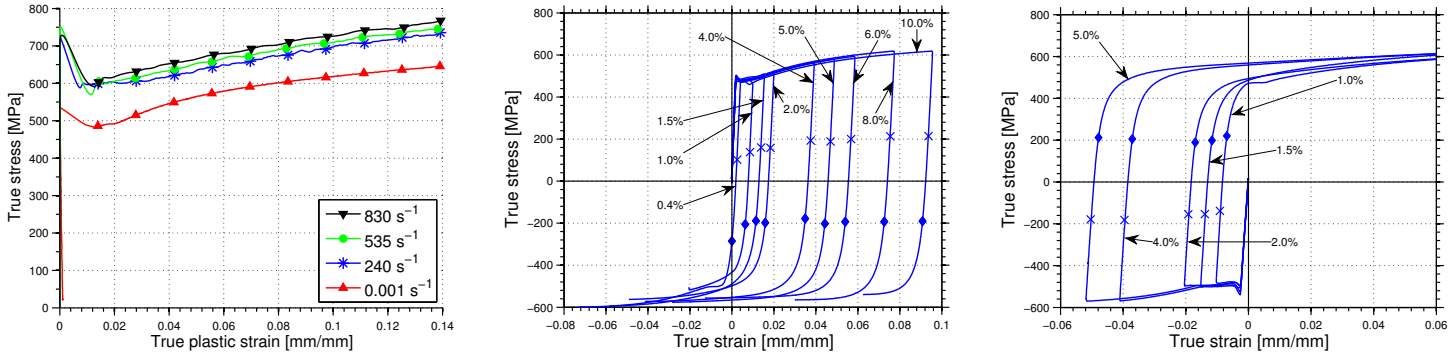

(a) Dynamic tests (b) Tension-compression (c) Compression-tension

FIGURE 4. DATA FROM SHTB TESTS (a), AND QUASI-STATIC REVERSED LOADING TESTS ON AXISYMMETRIC SPECIMENS (b)-(c).

the impact phase, necessitating information on the material's behaviour at elevated strain.

The fracture strain ε_f was calculated using Eqn. (2) by inserting the initial diameter D_0 and the diameter at fracture D_f when calculating A_0 and A. Both the initial and fracture diameters were measured using the laser device.

Reversed loading tests

To examine the isotropic and kinematic hardening properties of the material, experiments using reversed loading were performed. During impact, the pipeline suffers reversed loading with both compression before tension and vice versa. Specimens with geometry as shown in Fig. 2(c) were loaded in tension to a predefined level before the loading was reversed into compressive yielding (TC). Specimens were also loaded oppositely (CT). Compressive strains had to be kept below a certain value to avoid buckling and/or barrelling of the specimen. Specimens subjected to tension first were loaded to the true strain levels listed in Table 1 before reversing the load to compression, totalling nine specimens. Five specimens were loaded in compression first. In addition, one specimen was loaded to failure in tension only in order to obtain data on the onset of diffuse necking so this could be avoided in subsequent tests.

Test data are plotted in Fig. 4(b), showing the tension-compression tests, and in Fig. 4(c), which shows the compression-tension tests. Kinematic hardening is indeed present in the material, as indicated by the well-known Bauschinger effect. The diamond shaped markers denote the point of re-yielding after the load is reversed, while the crosses mark the center of the elastic domain. Re-yielding is defined to occur when the plastic strain accumulated after load reversal exceeds 0.005. There seemed to be no significant difference between which loading direction was applied first when loading to these strain levels. Right after re-yielding, the two specimens initially loaded to 0.4% in tension and 1.0% in compression displayed a level of constant stress before strain hardening occured. This is most likely caused by unloading during Lüders plateu. A more general observation is that all curves appear to converge for large strains.

COMPONENT TESTS

Setup

The experimental setup is an attempt to recreate the loading scenario where a pipeline is hit and displaced by an impacting object before being released and straightened as a consequence of rebounding caused by the presence of global axial forces. The experiments consist of two main steps: A simply supported pipe was first struck by a trolley with a given mass and velocity in a pendulum accelerator described in detail in [13]. Next, the pipe was straightened quasi-statically in a standard 1200 kN Instron tension machine using bolts through the unlathed end sections of the pipe, leaving it free to rotate. The former part represents the impact, while the latter is thought to correspond to the rebound and straightening of the pipe due to axial forces present in the pipeline. These steps are of course a simplification of the actual load events, but will serve as indicators as to what may happen in a real case and should capture the main physics. The main difference between the experiments and a real case is the absence of axial forces as the pipeline is deformed. In this paper two pipes – labelled A and B – were impacted at different velocities and subsequently stretched. A more compreshensive test programme is presented and compared in [17].

An actual piece of a pipeline was used as a test component. Vital test parameters, like the free span of the pipeline, the trolley's mass and the impact velocity, were designed by means of finite element simulations and the guidelines given in [6]. A schematic sketch of the impact test is shown in Fig. 5. It has been noted, as one might expect, that a pointed indenter may pierce the pipe more easily [18], therefore the sharpest indenter nose radius given in the guidelines was used (10 mm). Based on the guidelines and the simulations, a final test setup was decided on; the pipe was given a span of 1000 mm and a nominal wall thickness of 4 mm, resulting in a D/t ratio of about 30. This ratio is about the same as in many pipelines in use for oil and gas transportation [2] as well as in the tubes used in [7]. To achieve this D/t-ratio, and to ensure sufficient plastic deformation, the pipe was lathed down from 9.5 mm to 4 mm, thus introducing a somewhat rough surface, and a slightly uneven thickness over the cross-section. As noted in [17], the rough surface is believed to be of minor importance with respect to the global deformation and the fracture process. The pipes' thicknesses were measured by a portable ultrasound device and measurements were taken at specific locations forming a consistent grid.

The trolley was assigned a mass of 1472 kg and an initial velocity v_0 of 3.24 and 5.13 m/s for pipe A and B respectively, representing the velocity of a trawl boat towing the mass [6]. Fig. 6 shows the test setup, where (a) shows the impact part and (b) the stretching phase after the impact. The supports in the impact phase were massive cylinders with a diameter of 50 mm, while the nose of the trolley had a radius of 10 mm. A load cell located between the nose and the trolley was used to sample the contact force during impact [13]. In addition, buffers were set up to limit

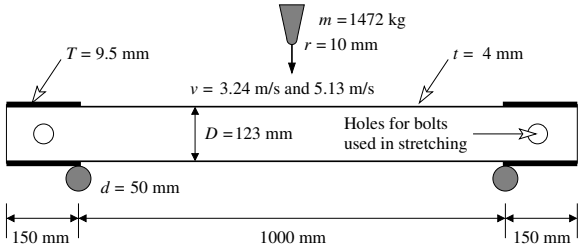

FIGURE 5. SCHEMATIC SKETCH OF THE IMPACT TEST.

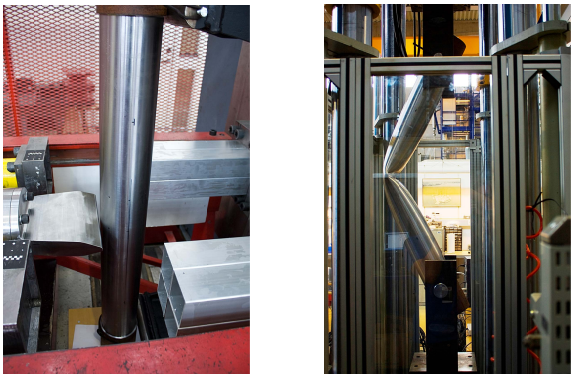

(a) Impact testing (b) Stretch test of pipe B

FIGURE 6. THE COMPONENT TESTS' (a) IMPACT PHASE AND (b) STRETCH PHASE.

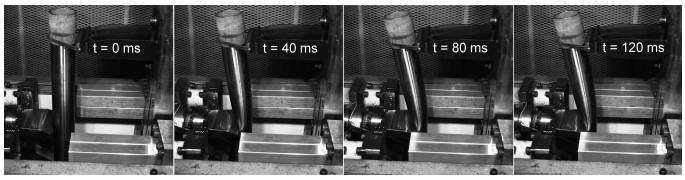

(a) Pipe A, v_0 = 3.24 m/s

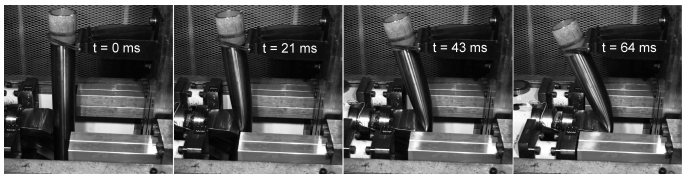

(b) Pipe B, v_0 = 5.13 m/s

FIGURE 7. THE IMPACT PHASE OF THE COMPONENT TESTS, WHERE (a) SHOWS PIPE A AND (b) PIPE B.

the maximum transverse deformation of the pipes.

Experimental results

Photo series at 5000 frames per second obtained by a high-speed camera of type FASTCAM SA1.1 model 675K-M1 can be

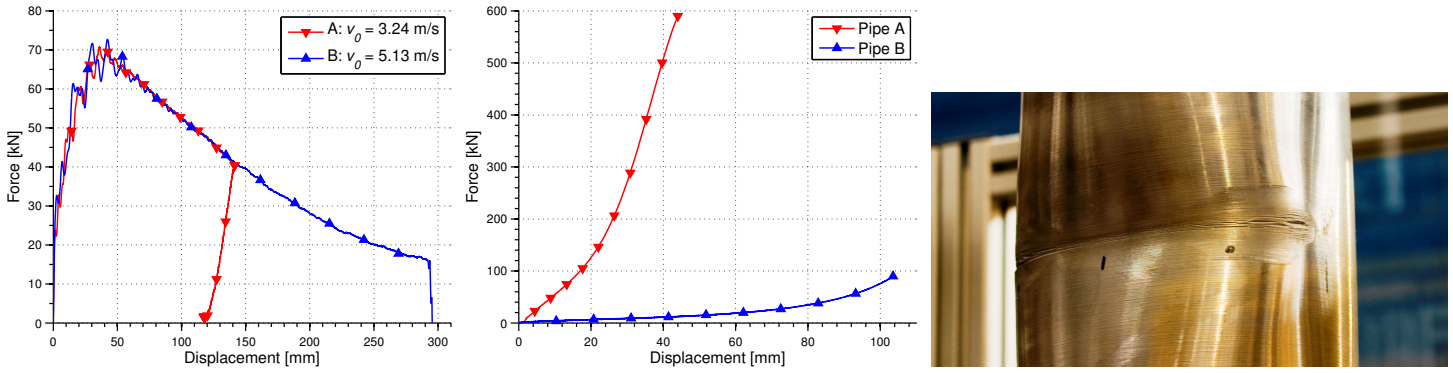

(a) Impact data (b) Stretch data (c) Fracture in pipe A

FIGURE 8. RESULTS FROM (a) IMPACT TESTS, AND (b) STRETCH TESTS. IT SHOULD BE NOTED THAT THE STRETCH DATA DOES NOT ACCOUNT FOR THE INCREASED MOMENT ARM CAUSED BY THE DEFORMATION FROM THE IMPACT. FIGURE (c) SHOWS SURFACE CRACKS IN PIPE A AFTER THE COMPLETE LOAD CYCLE.

seen in Figs. 7(a) and 7(b), which show the impact test of pipes A and B, respectively. Force-displacement curves for pipes A and B during both impact and subsequent stretching are plotted in Figs. 8(a) and 8(b). The force increases in the beginning of the impact when the deformation is still local, and starts to decrease when a transition is made from local to global deformation, which suggests an explanation for the peak loads being similar despite the different initial velocities. The remainder of the kinetic energy after the peak is attained, is mainly absorbed by global deformation. Note that in the test of pipe B, the trolley hit the buffer in the rig.

The deformation pattern observed corresponds well with the three modes of deformation identified by the quasi-static three-point bending tests on tubular components with similar D/t-ratio in [7]. These modes are crumpling, crumpling and bending, and finally structural collapse.

From Fig. 8(b) it is clear that higher initial velocity, and thereby higher deformation after impact, produces a much lower force level during stretching. When the stretching phase initiates, the least deformed pipe can take the applied load as axial forces almost immediately, while the most deformed one has to withstand a bending moment first due to their large global deformation. After being straightened, the oval shape of the pipes became quite circular, which can make impacted zones hard to detect underwater, especially if no visible cracks are present.

In the impact phase, the pipe was aligned so that it was struck on the side labelled north. Fracture was observed by visual inspection in both pipes during the stretch phase, but at very different load levels. Pipe B ruptured through the entire thickness of the pipe wall (Fig. 11) while pipe A seemed to only suffer superficial cracks and not through-thickness failure (Fig. 8(c)).

NUMERICAL SIMULATIONS

Constitutive relations and fracture criterion

Two different constitutive models have been used in this study; one with isotropic hardening only and another with combined isotropic/kinematic hardening. Both models are compared to each other and validated against the experimental data. The same fracture criterion has been employed in all analyses.

Johnson-Cook constitutive relation. The classical Johnson-Cook (JC) constitutive relation [19] is isotropic only, and is modelled with the von Mises yield criterion and the associated flow rule. The von Mises equivalent stress is a function of the deviatoric part of the Cauchy stress tensor $\boldsymbol{\sigma}$,

$$\sigma_{eq}(\boldsymbol{\sigma}) = \sqrt{\frac{3}{2}\boldsymbol{\sigma}^{\text{dev}} : \boldsymbol{\sigma}^{\text{dev}}} \tag{4}$$

The JC flow stress σ_{JC} is expressed as

$$\sigma_{JC}\left(\varepsilon_{eq}, \dot{\varepsilon}^*_{eq}, T^*\right) = \left(A + B\varepsilon^n_{eq}\right)\left(1 + C\ln\dot{\varepsilon}^*_{eq}\right)\left(1 - T^{*m}\right) \tag{5}$$

where ε_{eq} is the equivalent plastic strain, and A, B, n, C and m are material constants. The dimensionless plastic strain rate is given by $\dot{\varepsilon}^*_{eq} = \dot{\varepsilon}_{eq}/\dot{\varepsilon}_0$, where $\dot{\varepsilon}_0$ is a user-defined reference strain rate. The homologous temperature is defined as $T^* = (T - T_r)/(T_m - T_r)$, where T is the absolute temperature, T_r is the ambient temperature and T_m is the melting temperature of the material. This problem is assumed to be isothermal, thus omitting the temperature bracket of Eqn. (5) and reducing the model:

$$\sigma_{JC}\left(\varepsilon_{eq}, \dot{\varepsilon}_{eq}\right) = \left(A + B\varepsilon^n_{eq}\right)\left(1 + C\ln\frac{\dot{\varepsilon}_{eq}}{\dot{\varepsilon}_0}\right) \tag{6}$$

Then, from Eqn. (4) and Eqn. (6), the dynamic yield function f_{JC} becomes

$$f_{JC}(\boldsymbol{\sigma}, \varepsilon_{eq}, \dot{\varepsilon}_{eq}) = \sigma_{eq}(\boldsymbol{\sigma}) - \sigma_{JC}(\varepsilon_{eq}, \dot{\varepsilon}_{eq}) \tag{7}$$

where $f_{JC} = 0$ implies a possibility for viscoplastic behaviour, while $f_{JC} < 0$ means elastic behaviour. The initial size of the yield surface, i.e. when the equivalent plastic strain is zero, is given by the constant A.

Combined isotropic/kinematic model. The von Mises yield criterion and the associated flow rule are also used for the combined model, along with a backstress tensor $\boldsymbol{\alpha}$ to represent the translation of the yield surface due to kinematic hardening. The von Mises equivalent stress with respect to the backstress then becomes

$$\sigma_{eq}(\boldsymbol{\sigma} - \boldsymbol{\alpha}) = \sqrt{\frac{3}{2}(\boldsymbol{\sigma}^{\text{dev}} - \boldsymbol{\alpha}^{\text{dev}}) : (\boldsymbol{\sigma}^{\text{dev}} - \boldsymbol{\alpha}^{\text{dev}})} \tag{8}$$

Kinematic hardening and the evolution thereof, is described as

$$\boldsymbol{\alpha} = \sum_{i=1}^{N_\alpha} \boldsymbol{\alpha}_i\,, \qquad \dot{\boldsymbol{\alpha}}_i = \frac{C_i}{\sigma^0}(\boldsymbol{\sigma} - \boldsymbol{\alpha})\,\dot{\varepsilon}_{eq} - \gamma_i \boldsymbol{\alpha}_i \dot{\varepsilon}_{eq} \tag{9}$$

where C_i and γ_i are material constants, N_α is the number of backstresses and σ^0 is the size of the yield surface,

$$\sigma^0(\varepsilon_{eq}) = \sigma_0 + \sum_{j=1}^{N_V} Q_j\,[1 - \exp(-b_j \varepsilon_{eq})] \tag{10}$$

Equation (10) is the Voce hardening law in which σ_0 is the yield surface at zero plastic strain, Q_j and b_j are material constants, and N_V the number of terms included. Strain rate dependency is included multiplicatively by the yield ratio R

$$R(\dot{\varepsilon}_{eq}) = \left(1 + C \ln \frac{\dot{\varepsilon}_{eq}}{\dot{\varepsilon}_0}\right) \tag{11}$$

where C is the same as in Eqn. (6). The rate dependent data is entered as tabular data, with one curve for each strain rate. Abaqus interpolates logarithmically between each rate. Now the dynamic yield function f_C for the combined model is written out, combining Eqs. (8) and (11),

$$f_C(\boldsymbol{\sigma}, \boldsymbol{\alpha}, \varepsilon_{eq}, \dot{\varepsilon}_{eq}) = \sigma_{eq}(\boldsymbol{\sigma} - \boldsymbol{\alpha}) - \sigma^0(\varepsilon_{eq})\,R(\dot{\varepsilon}_{eq}) \tag{12}$$

As for the JC model, $f_C < 0$ indicates elastic behaviour while $f_C = 0$ signifies possible viscoplastic behaviour. This concludes the combined material model.

Fracture criterion. Finally, the Johnson-Cook fracture criterion was calibrated on basis of the notched (and smooth) tensile tests. The JC fracture strain ε_f is given by [20]

$$\varepsilon_f = [D_1 + D_2 \exp(-D_3 \sigma^*)]\left(1 + D_4 \ln \dot{\varepsilon}^*_{eq}\right)(1 + D_5 T^*) \tag{13}$$

where σ^* is the stress triaxiality as defined in Eqn. (3), and D_1 to D_5 are material constants to be calibrated. The damage parameter ω_D is defined as [21]

$$\omega_D = \sum_{k=1}^{N_{\text{inc}}} \frac{\Delta\varepsilon^{(k)}_{eq}}{\varepsilon_f} \tag{14}$$

Here, $\Delta\varepsilon^{(k)}_{eq}$ is the change of equivalent plastic strain in increment k and the summation is, as indicated, performed over all the increments in the analysis. Failure is said to occur when the damage parameter becomes equal to unity. As mentioned earlier, temperature dependency is omitted, i.e. $D_5 = 0$.

Identification of material constants

To determine the equivalent stress from the measured major principal stress σ_1 after necking, Bridgman's analysis [22] was employed

$$\sigma_{eq} = \frac{\sigma_1}{\left(1 + \frac{2R}{a}\right) \cdot \ln\left(1 + \frac{a}{2R}\right)} \tag{15}$$

The relation between the radius of the specimen's cross-section at the root of the neck, a, and the radius of the neck itself, R, were estimated by the empirical relation proposed by Le Roy et al. [23]

$$\frac{a}{R} = 1.1 \cdot (\varepsilon_{eq} - \varepsilon_U) \tag{16}$$

valid for $\varepsilon_{eq} > \varepsilon_U$ where ε_U is the equivalent plastic strain at the onset of necking. Material data from Figs. 3(a), 3(b) and 4(a) were then used to calibrate the JC model in Eqn. (6) and the Voce (isotropic) rule and rate dependent parts of Eqn. (12). Next, kinematic hardening was calibrated from the data from the reversed load tests in Figs. 4(b) and 4(c). The fracture strain ε_f was calibrated from the initial triaxiality of the notched specimens. All constants used in this study and details on the calibration can be found in [24].

Numerical model

Numerical simulations were carried out by the general purpose finite element code Abaqus [21], using the explicit solver.

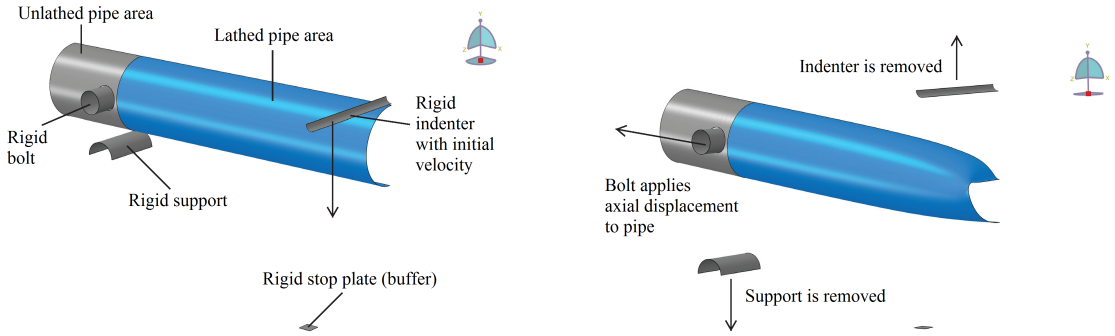

(a) Impact step (b) Stretch step

FIGURE 9. SKETCH OF GEOMETRIC MODEL USED IN NUMERICAL SIMULATIONS.

The simulations consisted of the entire load sequence from the component tests divided in two steps. As the stretch step is quasi-static in nature, rate effects were neglected and time scaling was applied to reduce the CPU time. Some simulation time was allowed to pass before initiating the stretch step to let the pipe come to rest. Different scaling factors were applied in a sensitivity study, and the effect of scaling was found to be negligible.

Due to symmetries, only a quarter of the experiment was modelled. The indenter, support and bolt were all modeled as discrete rigid shells, while the pipe was discretized using four-node quadrilateral reduced integration shell elements (with lengths of about the wall thickness) with hourglass control. A Simpson integration scheme was used with five integration points in the thickness direction of the shells. Eight-node linear brick elements, again with reduced integration and hourglass control, were also used to model pipe B for comparison with the shells. The lengths of the cubes were about $1 \times 1 \times 1$ mm in the impact zone, and had 2 to 3 times the length elsewhere. A sketch of the general setup is shown in Fig. 9. As the pipes had a varying thickness, average values based on the measurements were used.

An initial velocity was prescribed to the indenter, which also was assigned a mass of $1472/4 = 368$ kg. Contact between the pipe and the indenter, and the pipe and the support, was handled by a penalty based surface-to-surface algorithm. The contact force between the trolley and the pipe was sampled at even time intervals for validation against the experiments.

Numerical results

Impact on a global level was generally captured well by both the shell and volume models. Figure 10 shows high speed video images from pipe B, along with snapshots of the simulation with solid elements at corresponding times with a von Mises stress contour plot. Deformation shape, duration of the impact and strain localization (see Fig. 11) showed great compliance with the experiments. As seen in Fig. 12, the impact phase was also captured well in terms of the force-displacement curves. Both

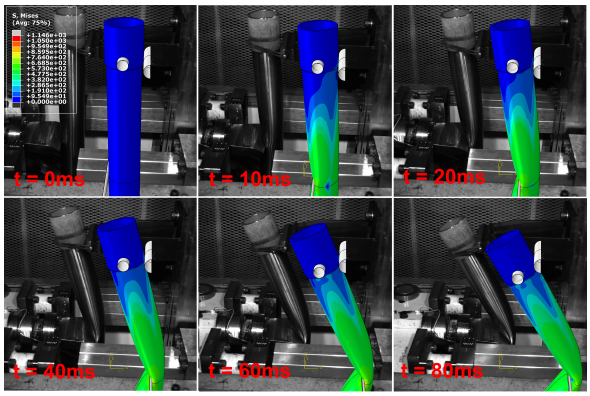

FIGURE 10. HIGH SPEED VIDEO AND SIMULATION RESULTS (JC SOLID MODEL) OF IMPACT OF PIPE B.

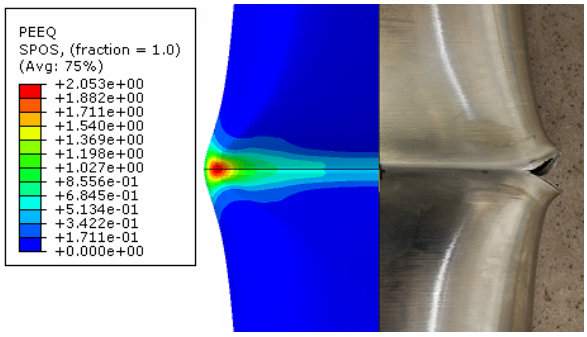

FIGURE 11. PIPE B AFTER IMPACT AND STRETCHING WITH EQUIVALENT PLASTIC STRAIN (JC SHELL MODEL).

material models, and both pipe discretizations performed well. For pipe B, the impactor hit the rigid buffer plate as in the experiments. Between the two material models, little difference was observed for the impact phase.

Figure 13 shows the force-displacement curve from the subsequent stretching of pipe B. It is clear that the force is somewhat

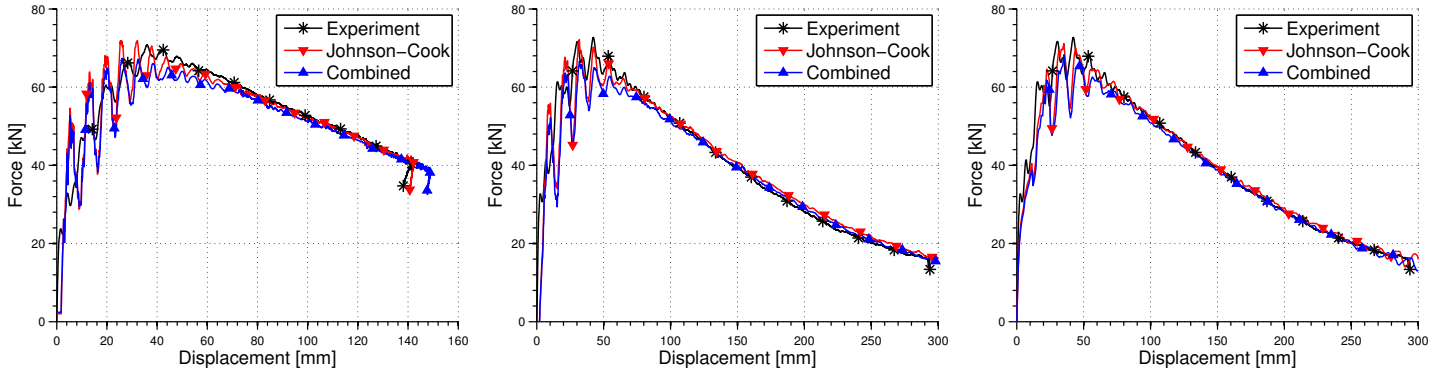

(a) Shell model pipe A (b) Shell model pipe B (c) Solid model pipe B

FIGURE 12. RESULTS FROM FINITE ELEMENT ANALYSES OF IMPACT PHASE.

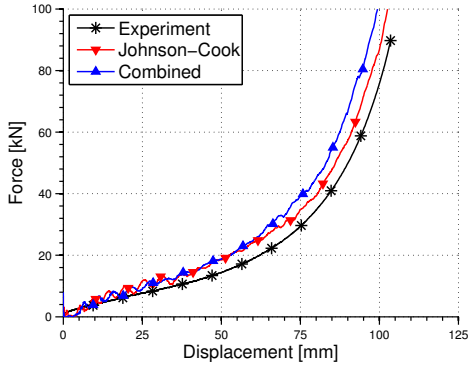

FIGURE 13. RESULTS FROM FINITE ELEMENT ANALYSES OF THE STRETCH PHASE OF PIPE B USING SHELL ELEMENTS.

overestimated compared to the experiments, with the combined material model (blue) and the JC model (red) performing equally well. Even though the pipe was allowed to "rest" before initiating the stretch step, some residual oscillations are present. This is more evident for pipe B due to the higher impact velocity. Initiation of contact between the bolt and the pipe also contributes to this. In the experiments, cracks were clearly visible in both pipes. The damage parameter ω_D never attained values sufficient for fracture, thereby causing an increased load level. As the critical areas of the pipe sustain large compressive strains at negative triaxialities during impact, not much damage is accumulated. When the load is reversed in tension, ω_D grows rapidly, but not enough to cause fracture.

DISCUSSION AND CONCLUDING REMARKS

The X65 pipeline material used can for engineering and design purposes be said to be both homogenous and isotropic. Notched tests revealed that the fracture strain decreased when the triaxiality increased, but the fracture stress remained of the same order. The material exhibits a strain rate dependency with increasing flow stress for increasing strain rates, a characteristic observed for many metals [25]. The dynamic component tests complied with the three modes of deformation identified in [7], even though the tests therein were quasi-static. Notwithstanding the similarities, deformation appeared to be more localized for the dynamic tests, although more tests should be conducted to confirm this assertion. Fracture was observed during stretching for both pipes; almost immediately for pipe B and at a later stage for pipe A. Higher impact velocity, i.e. larger deformation, forces the pipe to withstand the load as a bending moment rather than an axial load. When fracture is initiated, the effective cross-sectional area decreses and the capacity is further reduced.

Numerical simulations displayed excellent agreement with the impact experiments, in terms of force-displacement curves, local and global deformation, and duration. No large difference was detect between the two material models. On a global level, the shell model performed equally well compared to the solid model – at substantially less computational cost.

Stretching of the pipes, however, were not satisfactorily captured. Simulations showed a higher force level compared to the experiments for all models. This is most likely caused by the inability of the fracture criterion to predict the onset of failure in the material, a problem not encountered in [2] since no fracture was observed. Also, the tension machine's elastic stiffness is unaccounted for but has been shown to have a minor effect on these load levels [17]. All the material across the cross-section in the analysis is therefore available to carry load, resulting in an overestimation of the force. The varying stress state during the load sequence makes it hard to predict local strains accurately, and fracture even more so as it depends on equivalent plastic strain and stress triaxiality. As shown in [17], cracking of particles and/or void nucleation around particles appear to initiate fracture. Being a very local event, a micromechanical approach using unit cells may be well suited.

ACKNOWLEDGMENT

The present work has been carried out with financial support from the Research Council of Norway SIMLab – Centre for Research based Innovation (CRI) at the Norwegian University of Science and Technology. Thankful acknowledgement is made to Statoil ASA for supplying the test material. Contributions from M.Sc. students Kjetil Slåttedalen, Anders Ørmen, Jo Gaute Fornes and Steffen Gabrielsen are also greatly appreciated.

REFERENCES

[1] Jones, N., 2010. "Inelastic response of structures due to large impact and blast loadings". *Journal of Strain Analysis for Engineering Design,* ***45***, pp. 451–464.

[2] Manes, A., Porcaro, R., Ilstad, H., Levold, E., Langseth, M., and Børvik, T., 2012. "The behaviour of an offshore steel pipeline material subjected to stretching and bending". *Ships and Offshore Structures,* ***7***, pp. 371–387.

[3] Statoil ASA, Cited 23.01.2013. *Small gas leak from Kvitebjørn pipeline*. `http://www.statoil.com/en/NewsAndMedia/News/2008/Pages/gasleakkvitebjorn.aspx`.

[4] Jones, N., and Birch, R., 1996. "Influence of internal pressure on the impact behaviour of steel pipelines". *International Journal of Pressure Vessel Technology,* ***118***, pp. 464–471.

[5] DNV, 2008. *Offshore standard DNV-OS-F101: Submarine pipeline systems*. Det Norske Veritas.

[6] DNV, 2010. *Offshore standard DNV-RP-F111: Interference between trawl gear and pipelines*. Det Norske Veritas.

[7] Thomas, S., Reid, S., and Johnson, W., 1976. "Large deformations of thin-walled circular tubes under transverse loading – I: An experimental survey of the bending of simply supported tubes under a central load". *International Journal of Mechanical Science,* ***18***, pp. 325–333.

[8] Watson, A., Reid, S., and Johnson, W., 1976. "Large deformations of thin-walled circular tubes under transverse loading—II: Experimental study of the crushing of circular tubes by centrally applied opposed wedge-shaped indenters". *International Journal of Mechanical Science,* ***18***, pp. 387–397.

[9] Watson, A., Reid, S., and Johnson, W., 1976. "Large deformations of thin-walled circular tubes under transverse loading - III: Further experiments on the bending of simply supported tubes". *International Journal of Mechanical Science,* ***18***, pp. 501–509.

[10] Jones, N., Birch, S., Birch, R., Zhu, L., and Brown, M., 1992. "An experimental study on the lateral impact of fully clamped mild steel pipes". *Proceedings of IMechE, Part E: Journal of Process Mechanical Engineering*, pp. 111–127.

[11] Shen, W., and Shu, D., 2002. "A theoretical analysis on the failure of unpressurised and pressurised pipelines". *Proceedings of the Institution of Mechanical Engineers 216 (E)*, pp. 151–165.

[12] Oh, C.-K., Kim, Y.-J., Baek, J.-H., and Kim, W.-S., 2007. "Development of stress-modified fracture strain for ductile failure of API X65 steel". *International Journal of Fracture,* ***143***, pp. 119–133.

[13] Hanssen, A., Auestad, T., Tryland, T., and Langseth, M., 2003. "The kicking machine: A device for impact testing of structural components". *International Journal of Crashworthiness,* ***8***, pp. 385–392.

[14] Tenaris, Cited 23.01.2013. *Production processes*. `http://www.tenaris.com/AboutUs/ProductionProcesses.aspx`.

[15] Slåttedalen, K., and Ørmen, A., 2010. "Impact against offshore pipelines – Experiments and numerical simulations". Master's thesis, Norwegian University of Science and Technology.

[16] Chen, Y., Clausen, A., Hopperstad, O., and Langseth, M., 2011. "Application of a split-Hopkinson tension bar in a mutual assessment of experimental tests and numerical predictions". *International Journal of Impact Engineering,* ***38***, pp. 824–836.

[17] Kristoffersen, M., Børvik, T., Westermann, I., Langseth, M., and Hopperstad, O., 2013. "Impact against X65 steel pipes — an experimental investigation". *Submitted for possible journal publication*.

[18] Palmer, A., Neilson, A., and Sivadasan, S., 2006. "Pipe perforation by medium-velocity impact". *International Journal of Impact Engineering,* ***32***, pp. 1145–1157.

[19] Johnson, G., and Cook, W., 1983. "A constitutive model and data for metals subjected to large strains, high strain rates and high temperatures". *Proceedings of the 7^{th} International Symposium on Ballistics*, pp. 541–547.

[20] Johnson, G., and Cook, W., 1985. "Fracture characteristics of three metals subjected to various strains, strain rates, temperatures and pressures". *Engineering Fracture Mechanics,* ***21***, pp. 31–48.

[21] SIMULIA, 2010. *Abaqus analysis user's manual version 6.10*.

[22] Hill, R., 1950. *The Mathematical Theory of Plasticity*. Oxford University Press.

[23] Le Roy, G., Embury, J., and Ashby, M., 1981. "A model of ductile fracture based on the nucleation and growth of voids". *Acta Metallurgica,* ***29***, pp. 1509–1522.

[24] Fornes, J., and Gabrielsen, S., 2011. "Impact against offshore pipelines". Master's thesis, Norwegian University of Science and Technology.

[25] Børvik, T., Hopperstad, O., Berstad, T., and Langseth, M., 2001. "A computational model of viscoplasticity and ductile damage for impact and penetration". *European Journal of Mechanics A/Solids,* ***20***, pp. 685–712.